

Transition Prediction Based on Linear Stability Theory with the RANS Solver for Three-Dimensional Configurations

Yayun Shi*, Raphael Gross†, Charles A. Mader‡ and Joaquim R. R. A. Martins§

University of Michigan, Ann Arbor, MI 48109, USA

An accurate, efficient, and automatic laminar-to-turbulent transition prediction framework is developed. The framework includes a laminar boundary layer code and a linear stability code coupled with a Reynolds-Averaged Navier–Stokes (RANS) solver. The framework is able to analyze transition induced by contamination at the leading edge, Tollmien–Schlichting waves or cross-flow instabilities and uses a correlation relationship to predict the transition location and transition length for laminar separation transition. Three typical configurations with experimental data from subsonic to transonic flow regimes have been simulated to investigate Reynolds number, the angle of attack and Mach number effects on the Tollmien–Schlichting and cross-flow instabilities. The simulated transition locations and pressure coefficient distributions agree well with available experimental data and demonstrate the effectiveness of the transition prediction tool.

I. Introduction

As fuel costs rise and environment regulations become more stringent, we must investigate the potential of new technologies in aircraft design to reduce drag as a means of reducing fuel burn. Since the skin friction drag accounts for 50% of the total drag for a typical swept-wing transport aircraft at cruise, and laminar skin friction can be up to 90% lower than turbulent skin friction, maintaining extended laminar flow on the wing surface is one of the most promising technologies to reduce drag. Three promising technologies for achieving laminar flow on the surface are natural laminar flow (NLF), laminar flow control (LFC), and hybrid fully laminar flow control (HLFC) method. NLF¹ aims at geometry shaping to obtain a proper pressure distribution to delay laminar to turbulent transition. LFC² uses a small amount of suction to stabilize the boundary layer velocity. HLFC³ combines a suction system at the leading edge with a following suitable pressure gradient. In recent year, adjoint-based design optimization has been widely used for aircraft design now available in several computational fluid dynamics (CFD) solvers.^{4–7} ADflow is a structured, multiblock and overset CFD code⁸ with an efficient adjoint method developed by Mader et al.^{7,9} and Lyu et al.¹⁰ Our objective in this paper is to develop aerodynamic shape optimization with laminar to turbulent transition based on ADflow.

This paper focuses on developing an accurate laminar to turbulent transition prediction method based on ADflow, and demonstrate that laminar to turbulent transition is predicted accurately and efficiently. There exist two popular types of transition prediction methods coupled with Reynolds-Averaged Navier–Stokes (RANS): semi-empirical e^N method based a stability equation, and methods based on transport equations. The state of art method is the e^N transition prediction approach, which is based on linear stability equations and can be coupled with RANS solver,¹¹ so we have adopted that method here. There are two approaches to obtain the boundary layer information as input for the linear stability solver. One method is to use the laminar boundary layer code (BL code), and the other is to extract the information from the RANS solution directly. These two approaches are illustrated in Figure 1. The laminar BL code requires

*Visiting Scholar, Department of Aerospace Engineering.

†Post-Doctoral Fellow, Department of Aerospace Engineering.

‡Research Investigator, Department of Aerospace Engineering, AIAA Senior Member.

§Professor, Department of Aerospace Engineering, AIAA Associate Fellow.

fewer grid points in the near-wall region, although it is restricted to fully attached flow. BL information from the RANS solution directly allows for the presence of a laminar bubble in the boundary layer, but the mesh required to determine transition must be of high quality, especially in the near-wall region. In general, the first option is coupled with a linear stability solver, while the second option is used for database transition method coupled with RANS solver, which is able to handle automatically transition prediction.¹² The coupled transition solver has been widely used in industrial applications, from 2D simple geometries to 3D complex configurations with the first option mainly in the low-speed.^{13,14} However, the e^N method is challenging to implement in a parallel computational architecture (Figure 1), requiring the boundary layer velocity transfer to the stability code and transition information return to RANS solver.

During the last few years, the correlation-based transition model relying on two transport equations has become widely used because it is built strictly on local variables and easy to couple with parallel computational RANS solver. This method was first introduced for turbomachine flow computation¹⁵ (2D flow, high turbulence level) and was extended to be able to simulate the cross-flow (CF) instabilities in some cases.¹⁶ However, since the method is only loosely based on the underlying physical mechanisms, it is not a good choice for industrial applications. The $k - k_L - \omega$ model based on the use of a laminar kinetic energy transport equation is also popular due to its simple pattern coupled with parallel computational capabilities.¹⁷ However, this method is only developed for stream-wise transition prediction and can not be used for laminar aircraft design. Based on the strengths of the transport equation method in terms of high computational parallelization and the strength of the e^N method in capturing the physical mechanism behind transition, Coder et al.¹⁸ developed the amplification factor transport equation. The amplification factor transport equation incorporates the linear stability theory in a manner compatible with modern parallel computational solvers. However, this method only captures the Tollmien-Schlichting (TS) instabilities, failing to capture the cross-flow instabilities which are significant for swept wings. Therefore, this method needs further development before it can be used for three-dimensional transition prediction.

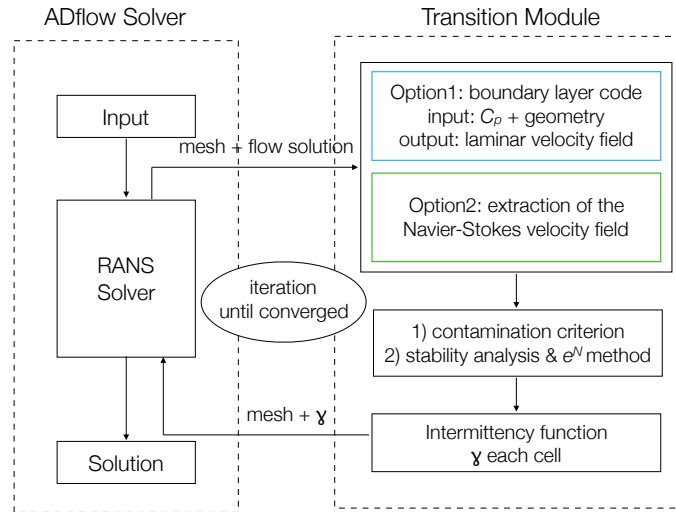


Figure 1. Transition prediction tool chain

We choose the e^N method, due to its practicality only contains the instabilities analysis, but also the contamination criterion and laminar bubble transition detection. The transition module includes a quasi-3D (conical assumption) boundary layer code, a linear stability equation code. Further, if contamination occurs at the attachment line, the whole wing will become turbulent, so a contamination criterion at the leading edge is considered in the e^N transition module as per Moens et al.¹⁹ To simulate the transition phenomenon of laminar separation, the laminar separation correction formula with either a short bubble or a long bubble is added in the e^N transition module as per Mayle et al.²⁰ The e^N method established in this paper is able to simulate laminar to turbulent transition caused by contamination attachment at the wing leading edge, TS waves, CF instabilities and laminar separation for natural transition in free flight condition with low external turbulence and noise levels, and good surface quality and can predict configurations from subsonic

to transonic. The full transition prediction chain is plotted in Figure 1 .

The rest of this paper is organized as three parts. First, in Section II, we introduce the transition model. Then, in Section III, we compare results from the new simulation framework with experimental data. Finally, We end with a summary of the conclusions in Section IV.

II. Methods

II.A. RANS solver

In order to accurately evaluate the Navier-Stokes velocity field and pressure, we use the high-fidelity aerodynamic solver ADflow. ADflow (formerly Sumb)²¹ is a second order finite-volume CFD solver that can solve structured, multiblock or overset meshes.²² ADflow initially solves a steady problem by time-marching schemes (Runge-Kutta algorithm or diagonalized diagonal-dominant alternating-direction implicit scheme) accelerated with multigrid to approach the initial iterate. The NewtonKrylov (NK) algorithm is started after the residual has dropped below a specified tolerance.²³ The solver computes aerodynamic functions of interest such as lift and drag, as well as the corresponding sensitivities of these functions using an efficient adjoint method implemented through Automatic Differentiation (AD) and developed by Mader et al.^{7,9} and Lyu et al.¹⁰ . Turbulence computations are carried out using the Spalart-Allmaras one equation model.²⁴

II.B. Transition criteria

We will focus on three types of transition mechanism for predicting laminar to turbulent transition: contamination at the attachment line, Tollmien-Schlichting (TS) waves and cross-flow (CF) instabilities.

The contamination at the attachment line is caused by the junction between the fuselage and the wing. The transport of the turbulence from the fuselage along the attachment line of the wing is enhanced by increased sweep angle and nose radius. When it occurs, the whole wing surface becomes turbulent. Therefore, it is necessary to determine whether or not the transition mechanism is caused by contamination. The attachment line contamination criterion¹⁹ is characterized by the parameter:

$$\bar{R} = w_e \sqrt{\nu \left(\frac{\partial u_e}{\partial x} \right)_{x_0}} \quad (1)$$

where x_0 refers to the attachment line, ν is kinematic viscosity, w_e is obtained by $w_e = q_\infty \varphi_{eff}$ (where q_∞ is freestream velocity and φ_{eff} is effective sweep angle of wing) and $u_e = \sqrt{q_\infty^2 - w_e^2}$. The critical value of the \bar{R} parameter is usually taken as 250 ± 20 . When $\bar{R} > 250 \pm 20$, contamination occurs and the whole wing surface becomes turbulent. Whereas when $\bar{R} < 250$, there is no contamination and the transition is predicted by the instability mechanism described in the following paragraph. Alternatively, momentum-thickness Reynold number Re_θ can be used to detect attachment-line contamination.¹⁹ It has been shown from similarity solutions on the attachment line that the relationship between Re_θ and \bar{R} : $Re_\theta = 0.404\bar{R}$.

In free-flight conditions, the transition is said to be natural. External disturbances or small average surface roughness will activate a phenomenon called receptivity. Receptivity describes the process through which instabilities are created in the BL. Instabilities are characterized by their frequencies, wavelengths, and the corresponding spatial growth rates. The TS waves are linked to the longitudinal velocity profile and amplified by an adverse pressure gradient, and, the CF instabilities are generated by the transverse velocity profile occurring with the favorable pressure gradient (e.g. close to the leading edge). These disturbances are amplified in the stream-wise direction until one reaches a critical amplitude, thus triggering the laminar to turbulent transition. We use linear stability theory to determine the growth rate of the instabilities and predict the natural transition.

In general, the laminar separation point is taken as transition point if amplification factor obtained from linear stability theory does not reach critical transition factor at upstream of the separation point. Mayle et al.²⁰ shows that the real transition location is downstream of the separation point. The separation bubble has two types, one is the short bubble, and another is the long bubble. The Reynolds number based on displacement thickness is used to distinguish the short and long bubble. If $Re_{\delta 1}$ is larger than 450,²⁰ we apply the short bubble criterion by using the Reynolds number base on the distance $(x_{Trbeg} - x_s)$:

$$(Re_x)_{sTrbeg} = 300Re_\theta^{0.7} \quad (2)$$

while for the long bubble, it is defined as

$$(Re_x)_{sTrbeg} = 700Re_\theta^{0.7} \quad (3)$$

When separation is close to the leading edge, it is easy to get a long bubble. We define the Reynolds number based on transition length with the following formula:

$$(Re_x)_{TrbegTrend} = 700Re_\theta^{0.7} \quad (4)$$

Then we can get the transition start point from Equation (2) or (3) and the transition length from Equation (4).

II.B.1. Linear stability theory

In our process we use the linear stability theory (LST)²⁵ which is based on a local analysis. We make the assumption that the boundary layer is not thickening locally (the flow is parallel locally). This assumption results in a linearization of NS equations. The flow can then be decomposed as the sum of the basic state q and a small disturbance \tilde{q} :

$$\tilde{q}(x, y, z, t) = q(y)e^{\alpha x + \beta y - \omega t} \quad (5)$$

where the prime indicates a perturbation quantity, q represents any of the flow variables, t is the time coordinate and x and z are the orthogonal spatial coordinates respectively normal and parallel to the leading edge. y is normal to the wing surface. q depends on y only. This approach is described by Schrauf²⁶ and leads to a system of second order differential equations, and forms a generalized eigenvalue problem with the condition:

$$f(\alpha, \beta, \omega, Re) = 0 \quad (6)$$

For simplicity and computational time, we use temporal theory to solve the problem in Equation (6) and use relation in Equation (7) from Schrauf et al.²⁷ to obtain the spatial amplification solution. The spatial amplification ratio is defined as:

$$\alpha_i = -\omega_i / \sqrt{\left\{ \frac{\partial}{\partial \alpha} \omega_r \right\}^2 + \left\{ \frac{\partial}{\partial \beta} \omega_r \right\}^2} \quad (7)$$

The frequency ω is complex and the wave number α and β are real, so the solution Equation (8) depends on five scalars ($\alpha, \beta, \omega_r, \omega_i, Re$):

$$\frac{d^2}{dy^2} q' + A(\alpha, \beta) \frac{d}{dy} q' + B(\alpha, \beta) q' = \omega C q' \quad (8)$$

A, B, C depend on basic flow values such as the local velocity and temperature profiles inside the boundary layer and their first and second derivatives.²⁵

II.B.2. N-factor integration strategies

With the spatial growth ratio α_i , the amplification factor is calculated as:

$$N_{factor} = \int \alpha_i ds \quad (9)$$

where s is the arc-length along the group velocity direction. We define two types of amplification factor: one for TS amplification factor which is related to frequency and in a propagation direction and one for CF amplification factor which is defined by frequency and wavelength. We obtain the TS N factor for a given frequency by integrating the amplification ratio in the inviscid direction. The envelope N_{TS} is determined by taking the maximum of the TS N factor evaluated for a wide range of frequencies at each location. For CF, we distinguish two types of waves: stationary waves and traveling waves. When the turbulence level of the freestream flow is small (turbulence intensity $Tu < 0.002$),^{28, 29} the stationary cross-flow instabilities play a dominant role on the rough wing surface, otherwise, traveling instabilities are dominant. Turbulent

intensity is low in the aerodynamic applications, therefore, we focus on stationary waves, and then the cross-flow factor is integrated by a constant wavelength with zero frequency. Similarly, the envelope N_{CF} is given by taking the maximum of the CF factor evaluated for a wide range of wavelengths at each location. The critical N_{crit_TS} value triggering the transition for TS waves is obtained by the Mack's relationship:³⁰

$$N_{crit_TS} = -8.43 - 2.4 \ln \frac{Tu(\%)}{100} \quad (10)$$

For CF instabilities, the critical N_{crit_CF} value is obtained using the experimental data from Crouch.²⁹ The critical value for CF instabilities not only depends on the turbulent intensity but also on surface roughness. The first envelope N factor (N_{TS} or N_{CF}) that reaches its critical value, is responsible for triggering laminar to turbulent transition.

II.C. Intermittency function

We use a continuous intermittency function (γ) to model the laminar to turbulent transition in ADflow.³¹ This is applied as a factor of the turbulence equation production terms. We decided to use a smooth intermittency function for the following reasons:

1. The preliminary computations with our BL code without γ showed some discontinuity in the pressure coefficient distribution corresponding to the transition location. This numerical artifact is due to the sharp transition between laminar and turbulent flows and could prevent the convergence of the transition position during coupling.
2. To compute the sensitivity of the flow we need to have a smooth solution.
3. It improves the convergence of the computation.
4. It also better represents the physics itself.

We generate transition region by defining γ :

$$\gamma(s) = 1 - e^{-0.413\xi^2} \quad (11)$$

with

$$\xi = \frac{3.36(s - s_{tr}^{beg})}{s_{tr}^{end} - s_{tr}^{beg}} \quad (12)$$

where s is the arc length starting at stagnation point and the ending point of the transitional region s_{tr}^{end} can be defined as:

$$s_{tr}^{end} = 2.3 \sqrt{\left(\frac{U_e}{\nu_e}\right)_{s_{tr}^{beg}} \delta_{(s_{tr}^{beg})}} + s_{tr}^{beg} \quad (13)$$

The boundary layer thickness δ is evaluated in boundary layer code. U_e and ν_e are tangential flow velocity and kinetic viscosity coefficient.

II.D. Coupling transition criteria with the RANS solver

There are two ways to start the transition simulation: either starting from a partially converged turbulent solution or from a laminar solution. We made the choice to start from a turbulent solution for a robustness reason. Trying to solve partially the laminar NS equation for a transonic configuration (presence of a strong shock wave) may lead to a jump in the residual. During the convergence process inside ADflow, we update the transition location whenever the magnitude of the density residual has been reduced to ε_ρ . When ε_ρ is taken below 10^{-3} , the pressure distribution changes little with different convergence order, so we take $\varepsilon_\rho = 10^{-3}$ to save the computation cost. We use an under-relaxed calculation to either move upstream or downstream and evaluate the new transition location:

$$x_f^{new} = x_f^{old} - \theta(x_f^{old} - x_p) \quad (14)$$

where θ is the relaxation factor, and x_f and x_p represent the forced and predicted transition points. By default we put θ equal to 0.95. We consider the iterative process converged when the maximum transition residual, $r_{tr} = \max|x_f - x_p|$, has converged to a tolerance of $\epsilon_{tr} = 10^{-6}$. If the transition procedure has converged, x_f is set as x_p , and the RANS solver with final transition location continues to converge until the magnitude of the density residual has reduced to a tolerance of $\epsilon_{pr} = 10^{-10}$.

III. Validation

We selected three different configurations with available wind tunnel data in order to validate the different transition scenarios possible. First, we simulate the infinite swept wing NLF(2)-0415 for subsonic flow with different Reynolds number (Re). Then, we show results for the M6 wing, also in subsonic flow at three different angles of attack. Finally, we simulate the Laminar Flow Model (LFM) airplane with transonic conditions for different angles of attack (AoA) and Mach numbers (M).

III.A. NLF(2)-0415, infinite span swept wing

The NLF(2)-0415 is an infinite swept-back wing which is tested in a low turbulence intensity ($Tu = 0.5\%$) wind tunnel.³² The wing sweep angle and the free-stream angle of attack are respectively fixed at 45° and -4° . We use a negative AoA to have a favorable pressure distribution to stabilize TS waves, while the CF instabilities are amplified. We performed the simulation with $M = 0.15$ for six different Re from $1.92e^6$ to $3.73e^6$. The reference chord (c) and the surface area are unitary ($c = 1.0\text{m}$, $s = 1.0\text{m}^2$). We run the simulation for a mesh composed of 281 grid points around the airfoil section, 121 points in the normal direction, 13 points in the span-wise direction. The grid ratio is 1.1 in the normal direction and y^+ is lower than 1. We simulate the infinite swept wing with the periodic boundary condition inside ADflow. Since the experimental data are only available on the upper surface, we do not display the results for the lower surface.

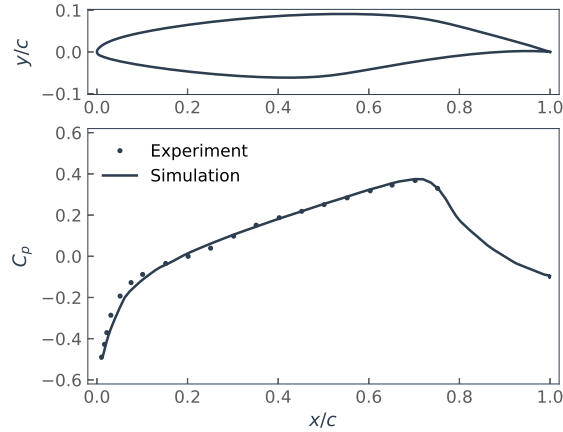


Figure 2. NLF(2)-0415 geometry and the designed pressure distribution

The NLF(2)-0415 airfoil section profile, the designed pressure distribution coefficient ($Re = 2.37e^6$) is plotted in Figure 2. The good agreement between numerical and experimental C_p shows that we are able to predict the transition location accurately. In Table 1, we present the contamination criteria results obtained with our transition framework for the last coupling (BL code + LST code + ADflow) for each Re . \bar{R} is lower than the critical value, so there is no contamination at the leading edge for each case and the wing can be analyzed with the transition criterion (e^N method).

Table 1. The contamination parameter \bar{R} vs. Reynolds number

Re	$1.92e^6$	$2.19e^6$	$2.37e^6$	$2.73e^6$	$3.27e^6$	$3.73e^6$
\bar{R}	145.596	150.979	161.494	170.171	184.091	196.156

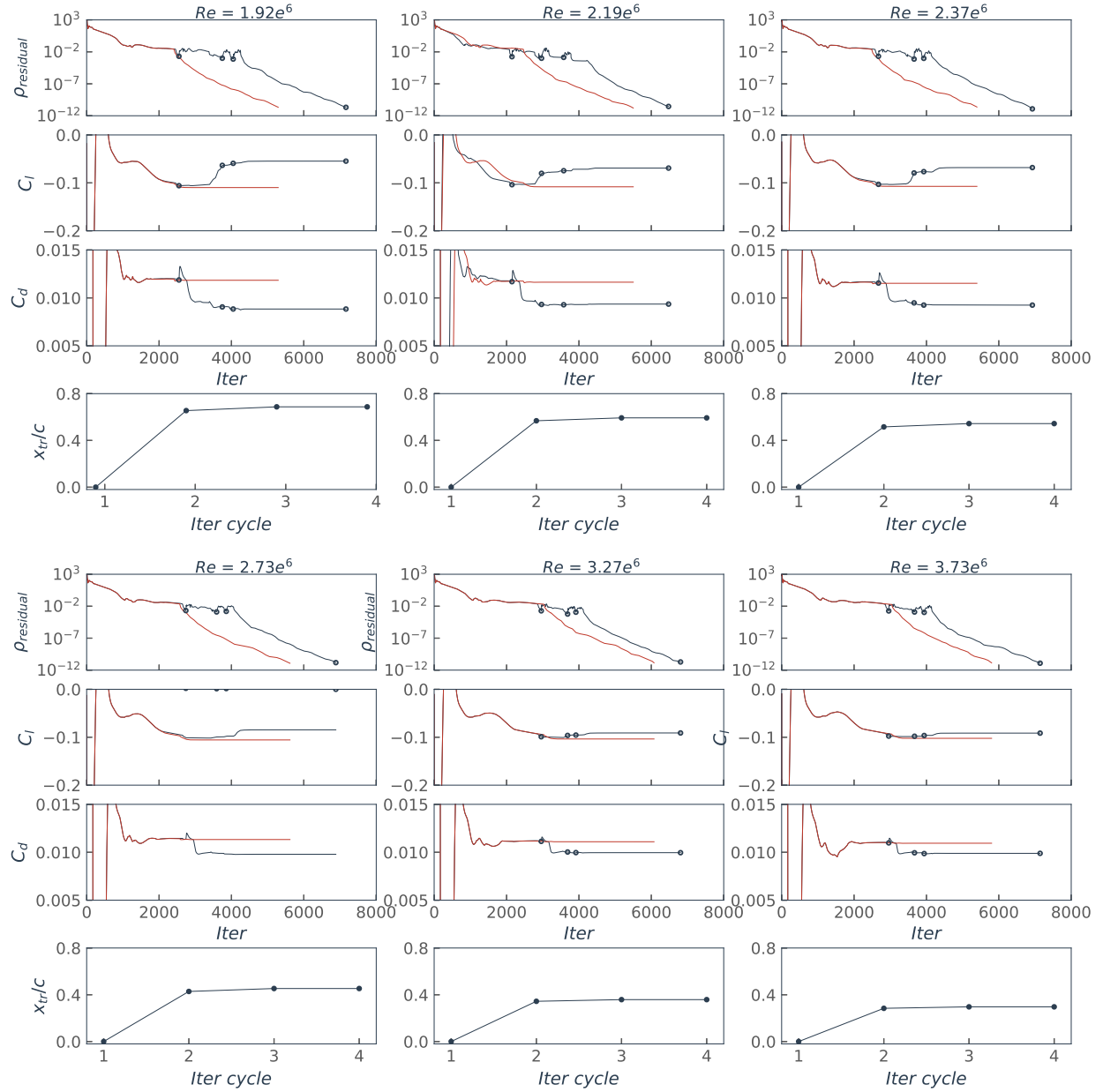


Figure 3. Convergence history at different Reynolds number, the black color is laminar to turbulent prediction while the red color is full turbulent calculation

Figure 3 shows the transition prediction convergence history (the density residual $\rho_{residual}$, the lift coefficient C_l , drag coefficient C_d and transition location x_{tr}/c) at different Reynolds number. The $\rho_{residual}$ converged to 10^{-10} and transition location residual on the upper surface converged to 10^{-6} . We focus on $Re = 2.37e^6$ case to analyze the transition iterations. The first transition location is 0 as we start from a fully turbulent simulation ($\gamma = 1$ for every cell of the mesh). Once the convergence of the $\rho_{residual}$ is small enough ($\rho_{residual} < 10^{-3}$), we update the transition location and γ function inside ADflow. The first transition location update needs the most iterations due to a large increase of laminar region from 0 to 0.543. While the second and third update need much fewer iterations to reduce $\rho_{residual}$ to 10^{-3} due to a small transition location movement and finally converged to $1e^{-10}$ with NK algorithm. The transition calculation iteration step is about 1.4 times of the turbulent case, so the increase of cost is sustainable compared with the fully turbulent simulation.

The critical amplification factor for TS waves is 9.0 decided by Equation (10) While CF critical factor is 8.5.³² For each Re , we show the converged transition analysis in Figure 4. In Figure 4 (a), we display the

amplification factors (N_{factor} , N_{TS} or N_{CF}) and also the critical values associated (horizontal grey lines). The transition location is detected whenever N_{factor} intersects its respective critical value. The pressure gradient being favorable to the development of CF instabilities for each Re study, all of the transition locations we detected are therefore induced by CF instabilities. In Figure 4 (b), we plot the transition location start points ($\gamma = 0$, red plain line) and the endpoints ($\gamma = 1$, red dashed line) obtained with the transition framework. The intermittency region corresponds to the length between the two red lines. Three different types of experiments results are available to us and are also presented in Figure 4 (b):

- Filled black square symbol for Naphtaline.
- Square symbol for hot wires.
- Triangle symbol for hot films.

The overall results seem in good agreement between the numerical and experimental results. However, a discrepancy of 4% of the chord can be seen for the lowest Re ($Re=1.92e^6$). This can be explained by multiple factors such as the assumption made with LST or the uncertainty around N_{crit_CF} as it is obtained from a set of experiments data.²⁹ Nevertheless, the discrepancy found has a relatively small impact on aerodynamic coefficient (0.5% of lift and 1% of drag).

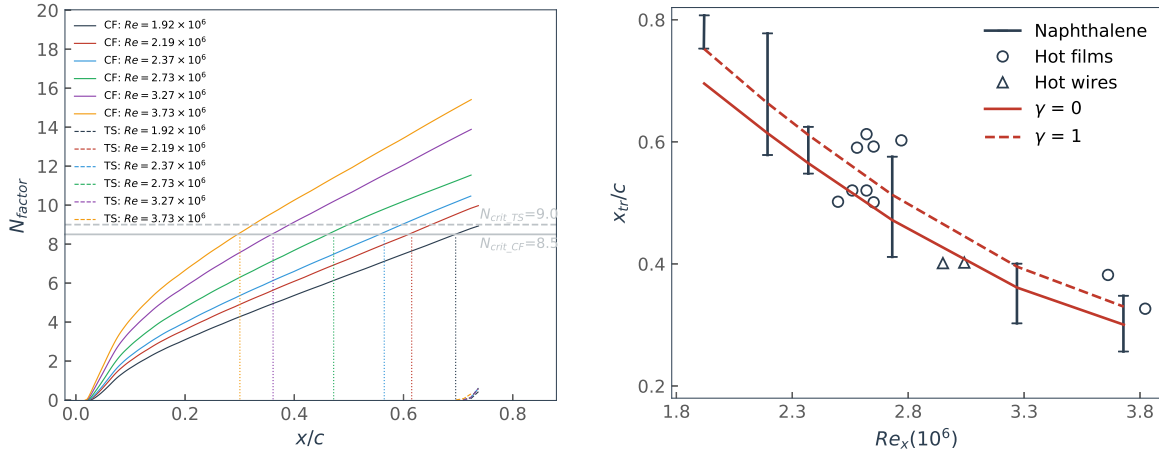


Figure 4. Amplification factor N_{factor} and transition locations (x_{tr}/c) comparison at different Reynolds number

III.B. ONERA M6 Wing

For M6 wing, we use the experimental flow condition³³ ($M = 0.262$, $Re = 3.5e^6$, $Tu = 0.2\%$) at three different AoA: 0° , 5° and 15° . The critical value of CF instabilities (N_{crit_CF}) is determined by matching the predicted transition location with the experimental data at AoA = 5° for a mid span section ($z/b = 0.45$). For TS waves, we use Mack's relationship to get the N_{crit_TS} . The reference chord (c) is 0.647m and the reference surface area (s) is 0.773m². The mesh composed of 281 grid points around the airfoil section, 121 points in the normal direction to make the grid ratio lower than 1.1 and 65 points in the span-wise direction. We have 12 sections to calculate the corresponding transition location and the slices are shown at the 15° in Figure 6 (b) on the upper surface. To make the results concise, we focus on four typical sections, which are $z_{span}/b = 0.1$, 0.45, 0.8 and 0.98 and marked with white color. The first step in our numerical process is to check the contamination criterion, which is listed in Table 2. All of the contamination parameters \bar{R} are lower than the critical value, so there is no contamination in the leading edge.

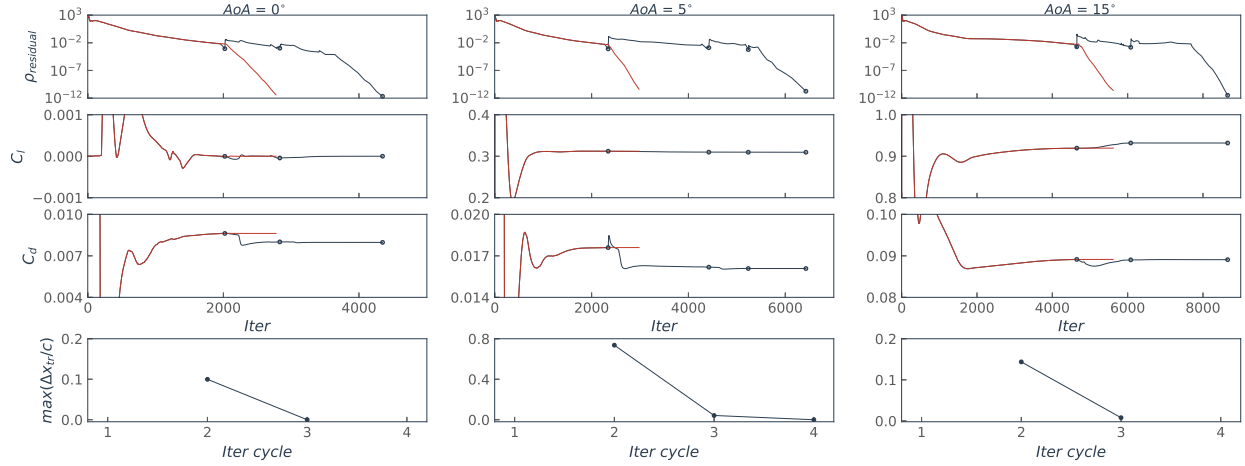


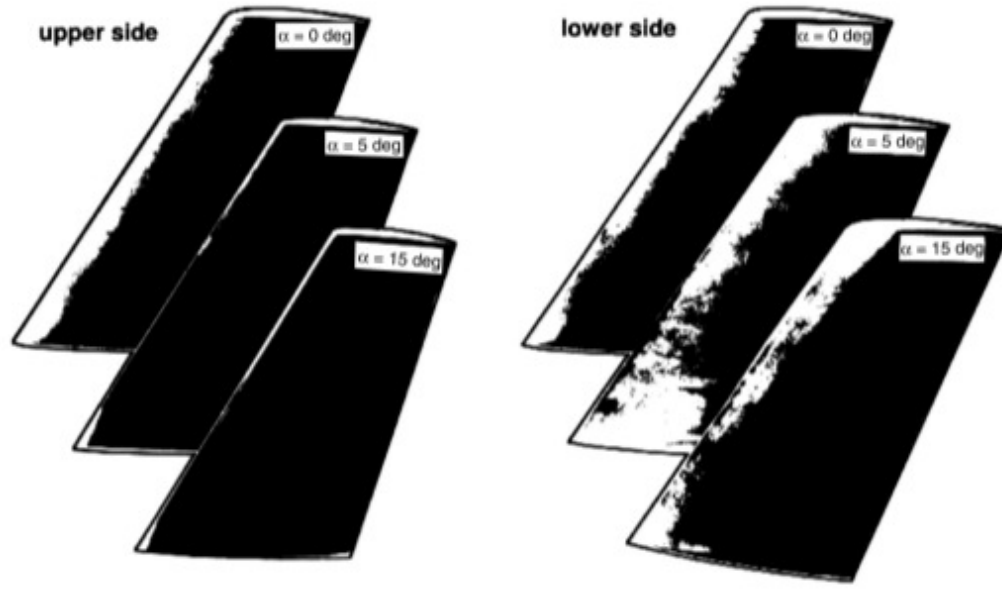
Figure 5. Convergence history at different angle of attack, the black color is laminar to turbulent prediction while the red color is full turbulent calculation

Table 2. Contamination paramters at different span-wise location for different angle of attack

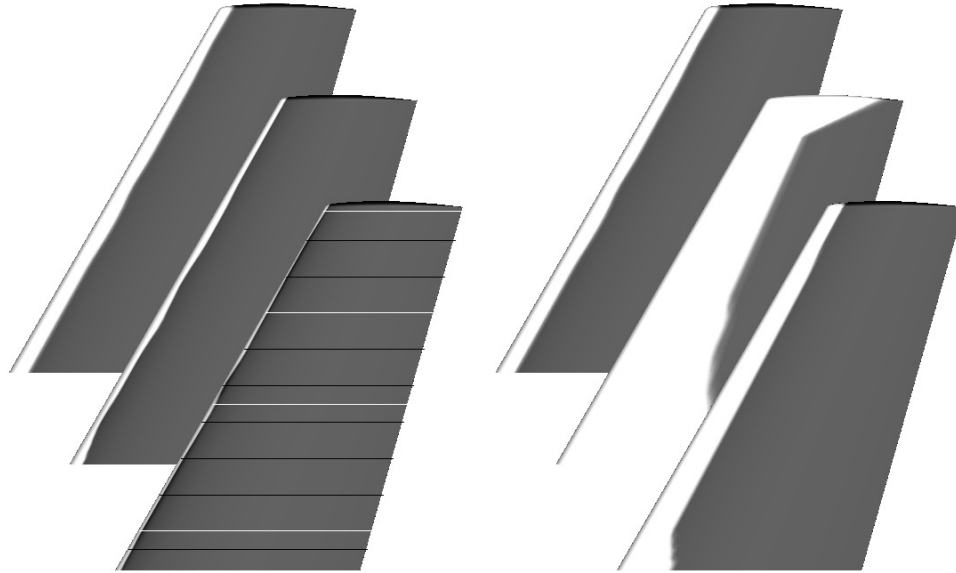
z_{span}/b	0.1	0.45	0.8	0.98
AoA = 0°	107.623	109.527	173.881	213.296
AoA = 5°	124.129	128.673	106.996	144.016
AoA = 15°	169.073	227.523	218.734	211.567

The convergence history (the density residual $\rho_{residual}$, the lift coefficient C_l , drag coefficient C_d and maximum transition location error $\Delta x_{tr}/c$) at different AoA is shown in Figure 5. For each span-wise section, there is the error between the predicted transition location and the forced transition location and we use the maximum error to check if the transition location converged ($max(\Delta x_{tr}/c)$). For 0° and 15° case, It needs 3 iteration cycle to converge with $\rho_{residual}$ and transition location residual lower than $1e^{-10}$ and $1e^{-6}$. For 5° case, it needs 4 iteration cycle to converge to the tolerance value. The second update of transition location moves downstream a lot on the lower surface with AoA = 5°, which leads to more iterations of the transition prediction with ADflow to converge. The maximum iteration step ratio between fully turbulent and transition prediction is about 2.2. In Figure 6 (a) and (b), we display the naphtalene experimental results³³ and our numerical results. The light color represents the laminar region while the dark region is turbulent region. It shows that the prediction transition locations are close to the experimental data except for the deviations at the wing tip.

Since the wing is made from a symmetrical airfoil, the results for AoA = 0° are symmetric. Therefore, we only display the result on the upper surface. The pressure coefficient distribution and the amplification factor are shown in Figure 7 (the dotted vertical line represents transition start location). The transition analysis shows that the strong adverse pressure distribution amplifies TS waves which will trigger the laminar to turbulent transition. The adverse pressure gradient increases from the root to the tip section, so the amplification factor has the same increment trend and the transition location moves upstream slightly. For the cases of AoA = 5° and AoA = 15°, we do not show the N_{factor} on the upper surface as the BL code detected the transition of the laminar bubble at the laminar separation close to the leading edge due to a sharp negative pressure gradient around $x/c = 0.01$ or 0.05 . Because the parameters $Re_{\delta 1}$ at the separation point are larger than 450, we use the short laminar bubble formula.



(a) Naphthalene distribution showing laminar and turbulent regions on the wing surfaces³³



(b) Intermittency distribution of the RANS simulation

Figure 6. Comparison of laminar/turbulent zone between numerical and experimental data for the ONERA M6 wing

For the case of 5° , we can see in Figure 8 that there are two stages in the front wing section on the lower surface. One is a sharp pressure decrease and the other one is a gentle pressure decrease. When it is close to the leading edge, the section at wing tip has the largest favorable pressure gradient, so the amplification factor of this section is larger than the others. However, the favorable pressure gradient changes after the leading edge and the section of $z_{span}/b=0.80$ has the largest favorable pressure gradient for a long distance. Finally, the integrated amplification ratio at the section of $z_{span}/b=0.80$ is the largest. Meanwhile, the amplification factor of the wing tip section isn't up to the critical value and the transition is induced by TS waves. The results agree with the conclusion that negative pressure gradient amplifies the CF stability. For the case of 15° , Figure 9 shows that all wing sections laminar to turbulent transition are caused by CF instabilities on the lower surface. The overall results show a reasonable agreement with the experiment and enable us to validate our transition framework.

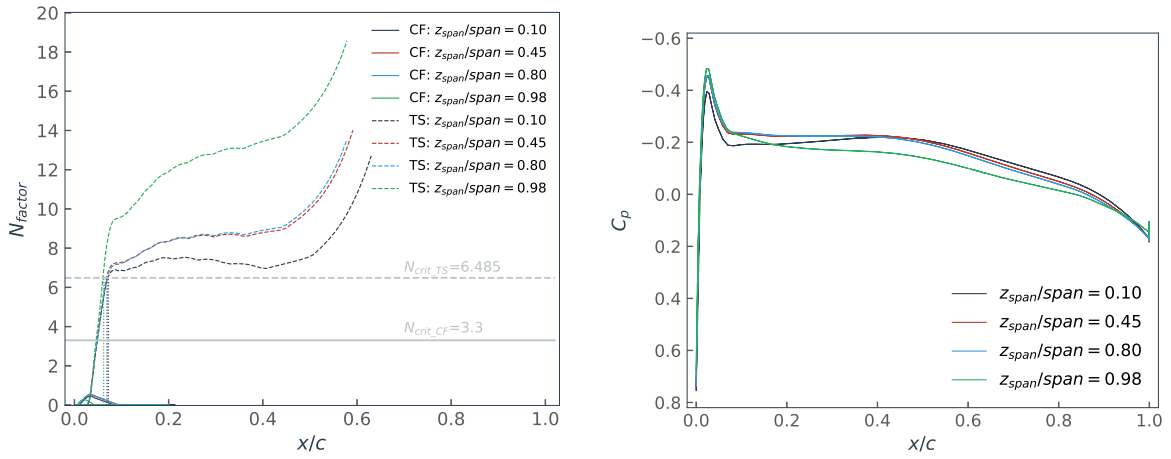


Figure 7. Amplification factor N_{factor} and pressure coefficient C_p distribution at 0° for M6 wing

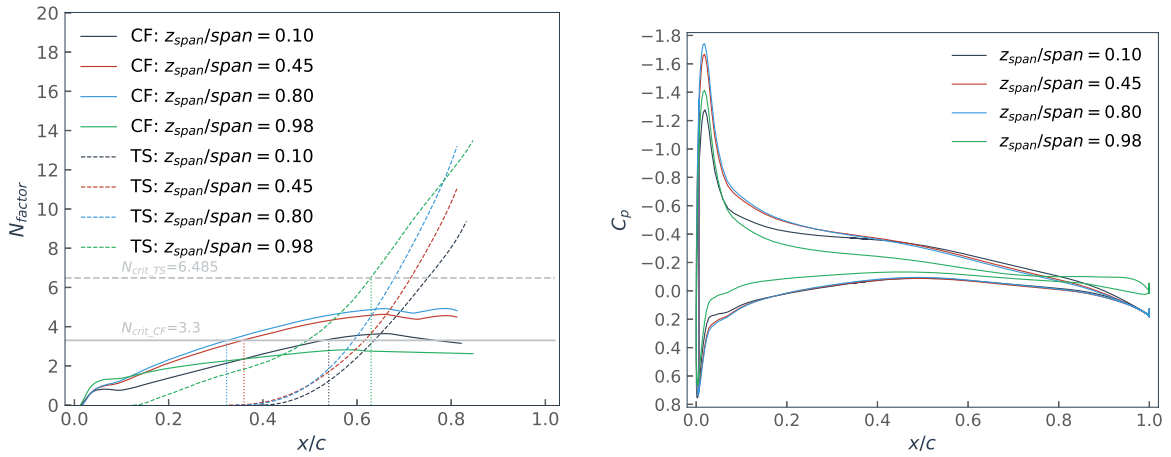


Figure 8. Amplification factor N_{factor} and pressure coefficient C_p distribution at 5° for M6 wing

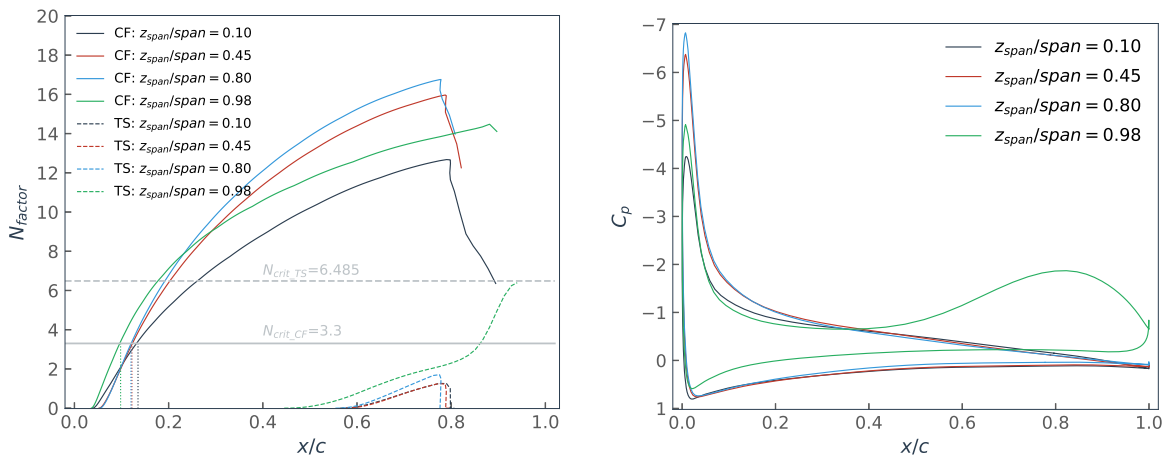


Figure 9. Amplification factor N_{factor} and pressure coefficient C_p distribution at 15° for M6 wing

III.C. Laminar flow model configuration

The laminar flow model (LFM) airplane is designed by Aircraft Research Association (ARA, UK) and Northwestern Polytechnical University (NPU, China). It is a tailless airplane made to research the natural laminar flow (NLF) and hybrid laminar flow control (HLFC) on a high swept wing (35°) in transonic. The airplane was tested in ARA wind tunnel during April 2017. The fuselage and the wing in the wind tunnel are shown in Figure 10. A description of the wind tunnel test is shown in Figure 11. The thermal insulation area ABS marked with green line is designed to capture transition phenomenon, while the red line region is the porous panel used for HLFC. The right green region is used for NLF transition analysis. In this paper, we focus on NLF transition analysis, so experiment data at span-wise direction $z = 1.05\text{m}$ is used for comparison with simulation results. The center of hot films sensors is used for taking laminar to turbulent transition pictures. There are three pressure taps lines to obtain the pressure distribution. The LFM has been tested with different M and AoA. We use an overset mesh of 10 million for the numerical simulation. The mesh characteristics are same as the previous case. There are 281 grid points around the airfoil section, 121 points in the normal direction to make the grid ratio lower than 1.1 and 65 points in the span-wise direction for the wing. y^+ is smaller than 1.0. The reference chord (c) is 0.562m and the reference surface area (s) is 0.8577m^2 . We get the $N_{crit_TS} = 6.485$ by using mack's relationship ($Tu = 0.2\%$). The N_{crit_CF} is obtained by matching the experiment result and numerical result at AoA = -0.15° and $M = 0.78$ case. The remaining cases use the same critical value.

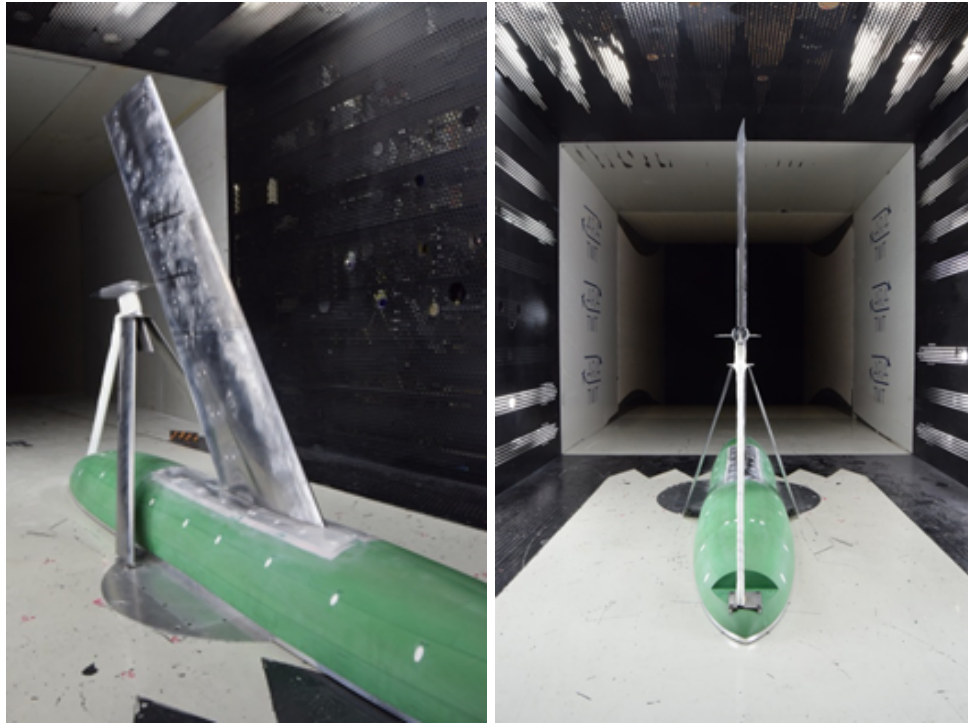


Figure 10. LFM model in the wind tunnel

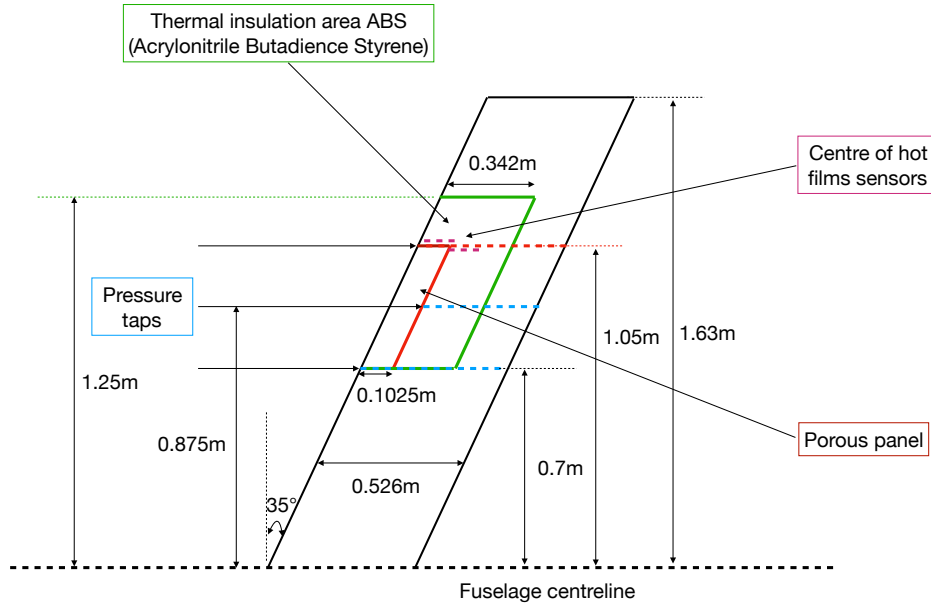


Figure 11. LFM dimensions and measurements locations

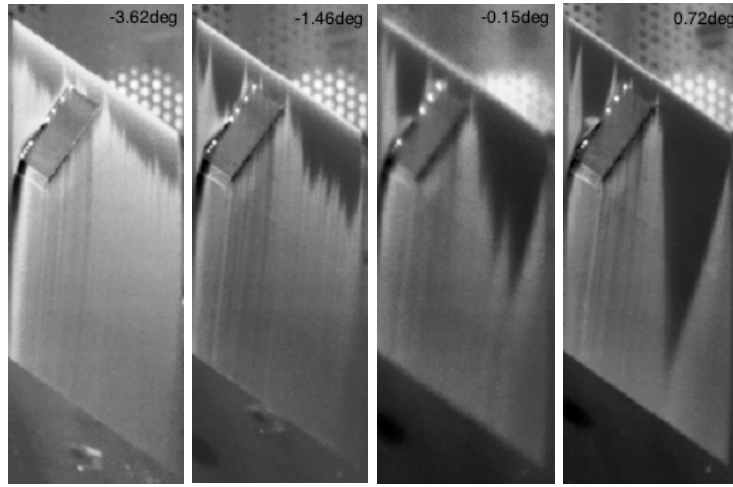
III.C.1. Angle of attack study

The study of AoA, we use the next conditions with ADflow: $M = 0.78$, $Re = 6.5e^6$, and $AoA = -3.62^\circ$, -1.46° , -0.15° , 0.72° . At first, we need to calculate the contamination criterion, which is in Table 3. The contamination parameters \bar{R} are listed on Table 3, so there is no contamination transition at all of the AoA.

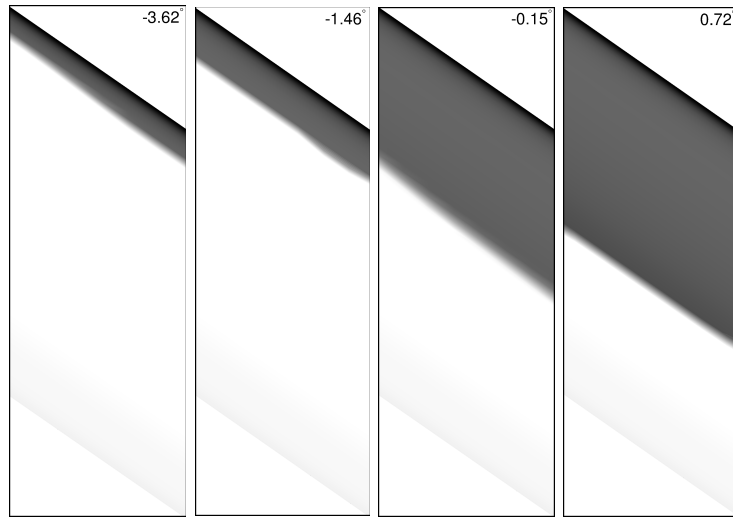
Table 3. Contamination paramters at $z_{span} = 1.05m$ for different angle of attack

AoA	-3.62°	-1.46°	-0.15°	0.72°
\bar{R}	162.784	131.646	124.673	115.602

We use Temperature Sensitive Paint (TSP) technology visualize boundary-layer transition from laminar to turbulent flow. The convective heat transfer coefficient (κ) in turbulent laminar flow is much higher than in laminar flow,³⁴ so within the turbulent boundary layer, a temperature change in the outer flow is transferred to painted wall faster than the laminar flow. A negative temperature change is used in this wind tunnel test, therefore, the lighter color of the infra-images represents the turbulent flow while the darker color represents the laminar flow. In Figure 12 (a) and (b), we display respectively the infra-red images from the wind tunnel test and the numerical result obtained by our framework. The wedge shape patterns represent premature transition, caused by inhomogeneity on the wing (holes, roughness, and hot films). The transition line can be seen as the borderline between dark and light areas. In Figure 12 (b), we show transition prediction results of RANS simulation (similarly, the dark color represents laminar flow while the light color represents turbulent flow). Both experiment results and simulation results show that transition location is shifted more and more downstream with increasing AoA. The transition starting and ending points are shown in Table 4. The experimental transition location and transition length are obtained by analyzing the infrared thermography results as the temperature has the difference from laminar to turbulent flow. The transition results of RANS simulation agree well with experimental data.



(a) Infra-red images



(b) Intermittency distribution of RANS simulation

Figure 12. Infra-red images of wind tunnel experimental data and the intermittency of transition simulation results at different angle of attack

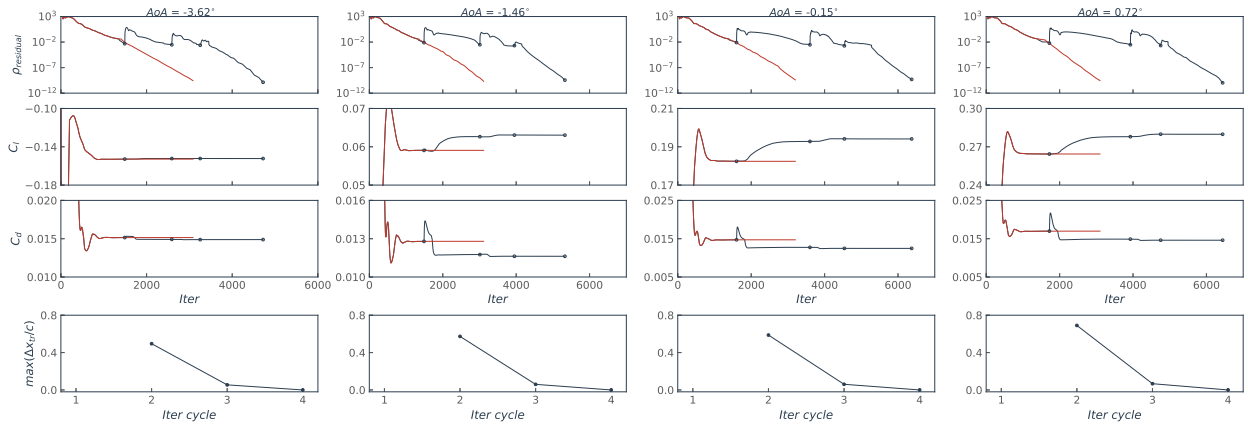


Figure 13. Convergence history for for LFM at different AoA with $M = 0.78$

The convergence history (the density residual $\rho_{residual}$, the lift coefficient C_l , drag coefficient C_d and

maximum transition location error $\Delta x_{tr}/c$) is plotted in Figure 13. The $\rho_{residual}$ of ADflow and the $\max(\Delta x_{tr}/c)$ are respectively up to $1e^{-10}$ and $1e^{-6}$. The transition prediction iteration steps is about 2 times longer than the full turbulent simulation, which is larger than the subsonic case.

Table 4. Transition region comparison

AoA	-3.62 °	-1.46 °	-0.15 °	0.72 °
Experiment Location (x/c)	0.08-0.09	0.14-0.17	0.37-0.45	0.57-0.58
Simulation Location (x/c)	0.085-0.11	0.14-0.18	0.40-0.49	0.565-0.574

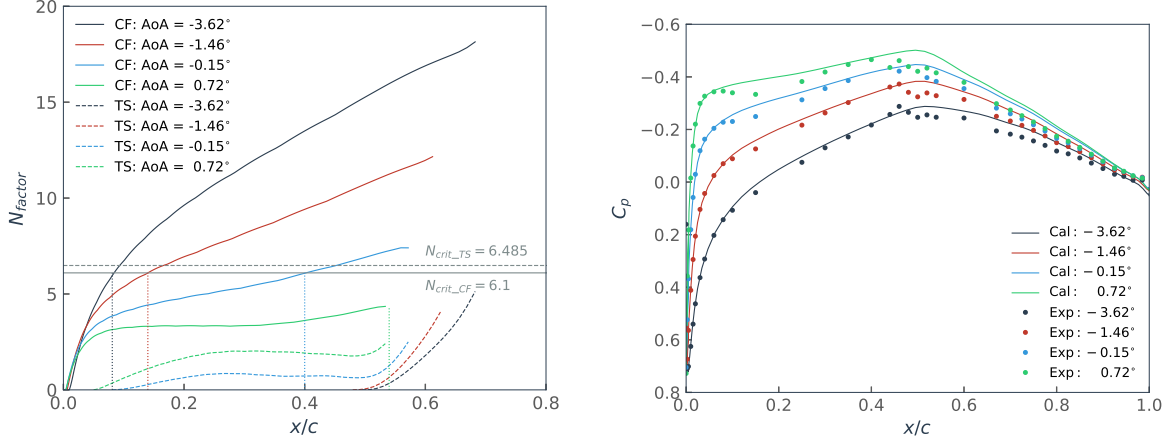


Figure 14. Amplification factor and pressure distribution for LFM at different angle of attack

For the three negative AoA, the transition is caused by CF instabilities (Figure 14 (a), the dotted vertical line represents transition start location). As the AoA increases, the transition location moves downstream for $x/c = 0.085$ (AoA = -3.62°) to $x/c = 0.40$ (AoA = -0.15°) due to decreasing favorable pressure gradient (Figure 14 (b)). In Figure 15, we display the local swept angle at the BL edge and the transversal velocity profile at $x/c = 0.1$. Both the CF velocity profile and the inflection point ($w''/w_e = 0.0$) affect the CF instabilities. An inflection point provides a source of an inviscid instability mechanism, and, the higher inflection point in the BL is, the larger CF instabilities are. As AoA increases, the local swept angle becomes smaller and the magnitude of the CF velocity profile gets smaller (Figure 15 (b)). Therefore, CF instabilities are less amplified. In Figure 15 (b), it shows the AoA has a huge influence on the CF velocity profile but low on the inflection point ($w''/w_e = 0$, the first three cases have the same inflection point, while the last case has a higher inflection point with one grid point in the normal direction), so the CF velocity profile is the dominant factor for the CF instabilities. For AoA = 0.72° (green line, Figure 14), CF instabilities do not trigger the transition anymore. The N_{factor} is much weaker due to a lower favorable gradient between $x/c = 0.1$ and $x/c = 0.4$. The critical value of $N_{crit_{TS}}$ is not reached before the BL code detected a laminar separation. Therefore, we use Equation (2) and Equation (4) to calculate the transition start location and transition length.

Even though experimental and numerical data seems to agree well with the transition location (Table 3), there are some small discrepancies for the C_p . There are several possible reasons for these discrepancies:

1. There is an error between digital model and manufactured model.
2. The model has an aeroelastic deformation in the process the wind tunnel tests.
3. Basically, there is an error between the experimental data and simulation data, especially in the transonic case.

The the second factor caused mainly the deviation.

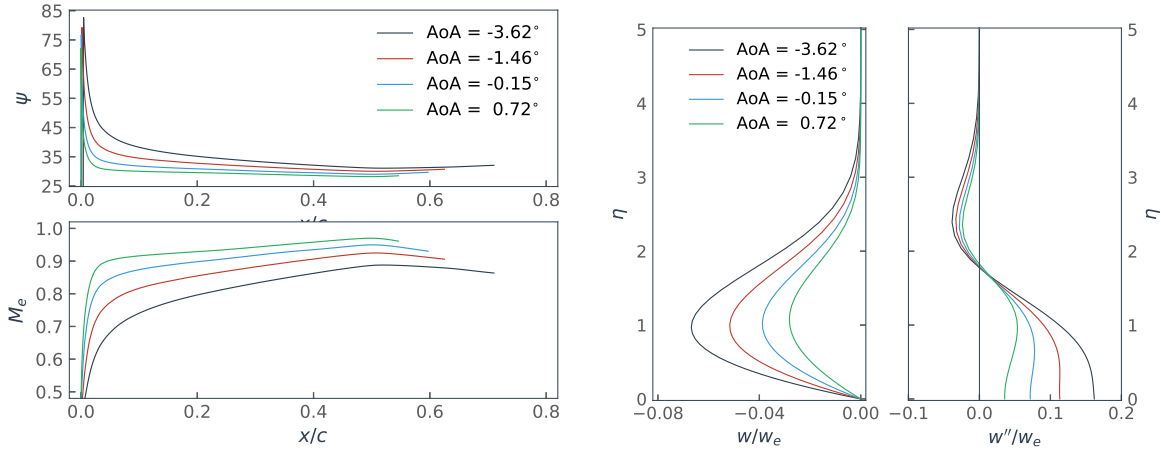


Figure 15. Local swept angle in the potential flow direction, Mach number at the boundary layer edge and CF velocities and the second derivatives at different angle of attack

III.C.2. Mach number study

The conditions are selected at $Re = 6.5 \times 10^6$, $AoA = -1.46^\circ$, and $M = 0.7, 0.78$, and 0.85 . The contamination parameters \bar{R} are $\bar{R}_{M=0.7} = 130.335$, $\bar{R}_{M=0.78} = 131.646$ and $\bar{R}_{M=0.85} = 133.435$, so there are no contaminations at the leading edge for all of angles of attack. The convergence history (the density residual $\rho_{residual}$, the lift coefficient C_l , drag coefficient C_d and maximum transition location error $\Delta x_{tr}/c$) is plotted in Figure 16. The iteration step of fully turbulent calculation is about 2 times of the transition prediction, which is considerable.

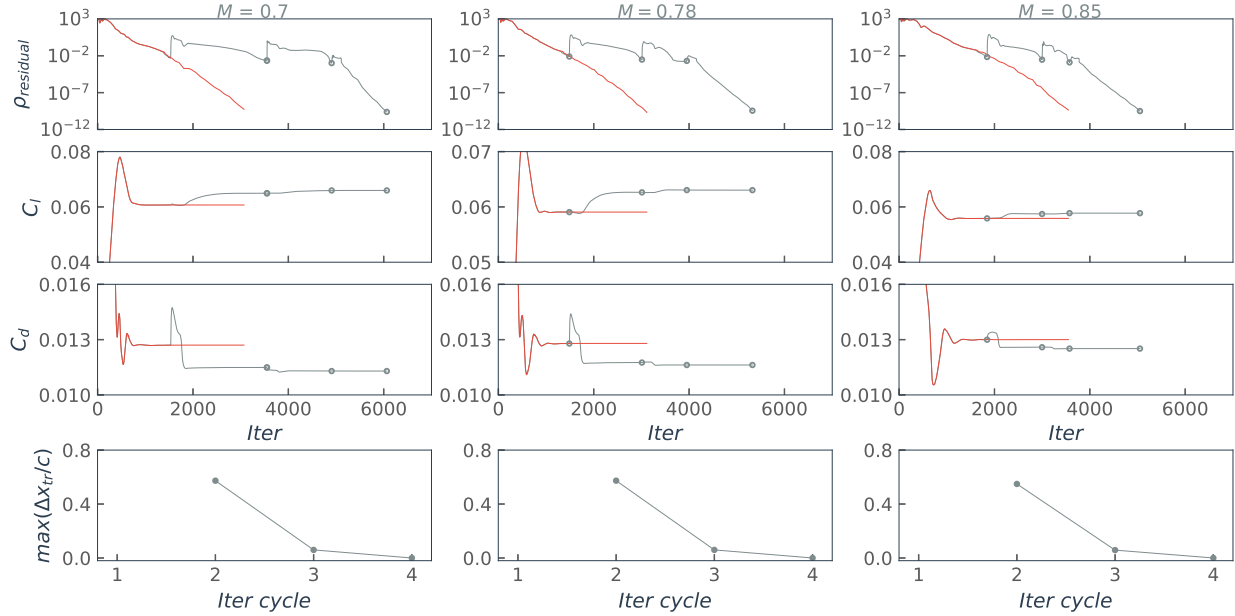


Figure 16. Convergence history for for LFM at different M with $AoA = -1.46^\circ$

The amplification factor and pressure coefficient distribution are shown in Figure 17. With increasing Mach number, the transition location moves upstream (Figure 17 (a), dotted vertical line represents transition start location) due to stronger favorable pressure gradient (Figure 17 (b)).

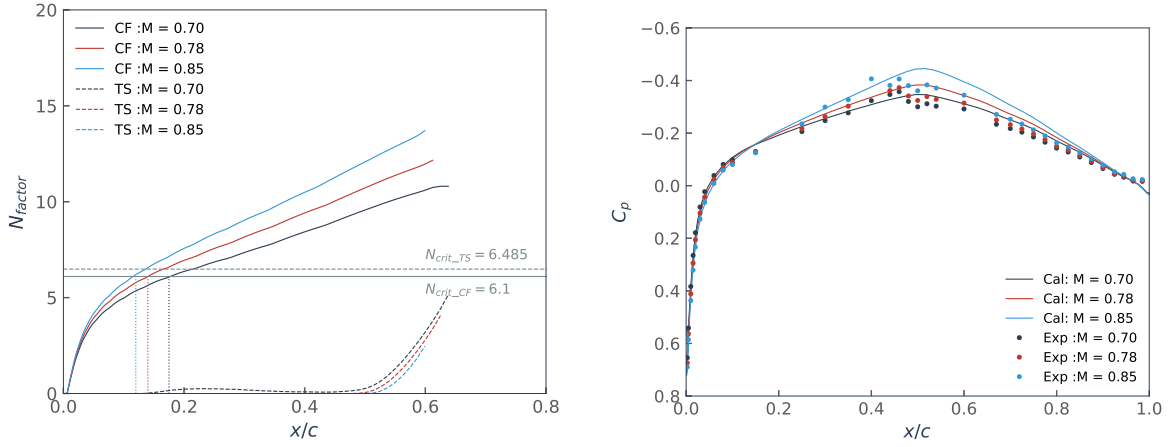


Figure 17. Amplification factor and pressure distribution for LFM at different Mach number

We plot respectively the local swept angle in the potential flow direction, the non-dimensional velocity M_e at the boundary layer edge and the CF velocity profiles and its second derivative (which is used to find the flection point) at $x/c = 0.1$ (Figure 18). With different M , the local swept angles almost are same for the three cases but M_e has a big difference, so M_e at the boundary layer edge decides the CF velocity profile at the streamwise direction. In Figure 18 (b), the inflection point has little difference and the CF velocity profile dominates the laminar to turbulent transition. It comes to a conclusion, When M number increases, it increases the cross-flow velocity profile and the transition location moves upstream.

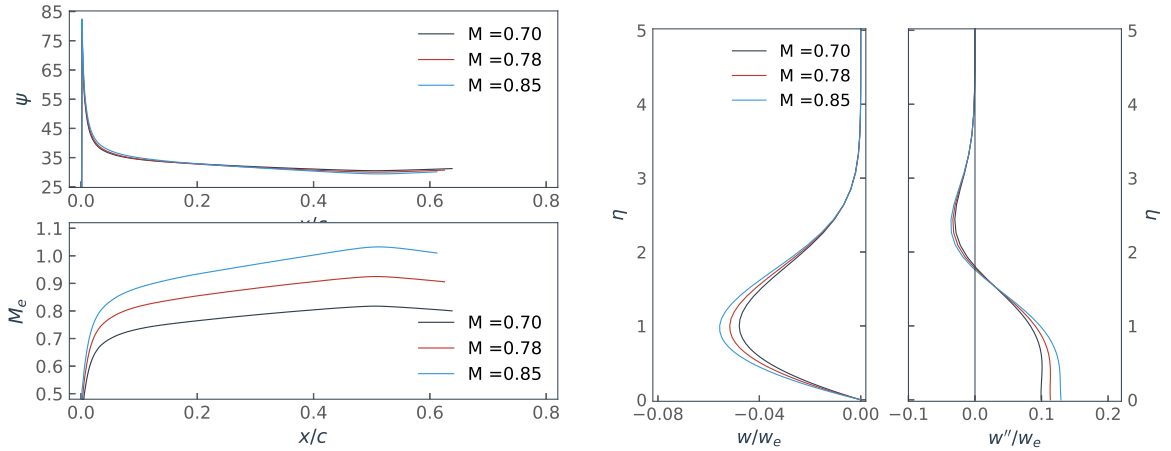


Figure 18. Local swept angle in the potential flow direction, Mach number at the boundary layer edge and velocities in the cross-flow and the second derivatives at different Mach number

LFM model has been used to study AoA and M effects on the laminar to turbulent transition. Both the AoA and M effect the pressure distribution and then effect the velocity profile in the boundary layer (especially the cross-flow velocity profile for LFM model).

IV. Conclusions

We developed a reliable transition prediction framework based on a RANS solver composed of a boundary layer code and a linear stability code. This framework is able to detect the contamination at the wing leading edge and predict natural transition induced by TS waves or CF instabilities. In the case of laminar separation, Mayle's correction criterion is used to predict the transition position and the transition length with a distinction between short and long bubbles. We simulate three configurations with developed framework. The NLF(2)-0415 and M6 wing configurations are subsonic cases and the results show the effects of Reynold number and angle of attack on transition location. The LFM configuration is a transonic case,

which shows the angle of attack and Mach number on transition location. All of the transition predictions in this paper agree well with the experimental data except some affordable derivations.

References

- ¹Eric Allison, Ilan Kroo, Peter Sturdza, Yoshifumi Suzuki, and Herve Martins-Rivas. Aircraft conceptual design with natural laminar flow. In *27th International Congress of the Aeronautical Sciences*, pages 2010–1, 2010.
- ²Ronald D Joslin. Overview of laminar flow control. 1998.
- ³Kristof Risse, Florian Schueltke, Eike Stumpf, and Geza Schrauf. Conceptual wing design methodology for aircraft with hybrid laminar flow control. In *AIAA 52nd aerospace sciences meeting (ASM)*, AIAA, National Harbor, MD, 2014.
- ⁴Tim Albring, Max Sagebaum, and Nicolas R. Gauger. *New Results in Numerical and Experimental Fluid Mechanics X: Contributions to the 19th STAB/DGLR Symposium Munich, Germany, 2014*, chapter A Consistent and Robust Discrete Adjoint Solver for the SU2 Framework—Validation and Application, pages 77–86. Springer International Publishing, Cham, 2016.
- ⁵Eric J. Nielsen and William L. Kleb. Efficient construction of discrete adjoint operators on unstructured grids using complex variables. *AIAA Journal*, 44(4):827–836, 2006.
- ⁶Markus Widhalm, Joël Brezillon, Caslav Ilic, and Tobias Leicht. Investigation on Adjoint Based Gradient Computations for Realistic 3d Aero-Optimization. In *13th AIAA/ISSMO Multidisciplinary Analysis and Optimization Conference*, number September, pages 1–17, Fort Worth, TX, 2010.
- ⁷Charles A. Mader, Joaquim R. R. A. Martins, Juan J. Alonso, and Edwin van der Weide. ADjoint: An approach for the rapid development of discrete adjoint solvers. *AIAA Journal*, 46(4):863–873, April 2008.
- ⁸Gaetan KW Kenway and Joaquim RRA Martins. Multipoint high-fidelity aerostructural optimization of a transport aircraft configuration. *Journal of Aircraft*, 51(1):144–160, 2014.
- ⁹AC Marta, CA Mader, JRRR Martins, E Van der Weide, and JJ Alonso. A methodology for the development of discrete adjoint solvers using automatic differentiation tools. *International Journal of Computational Fluid Dynamics*, 21(9-10):307–327, 2007.
- ¹⁰Zhoujie Lyu, Gaetan K. Kenway, Cody Paige, and Joaquim R. R. A. Martins. Automatic differentiation adjoint of the Reynolds-averaged Navier–Stokes equations with a turbulence model. In *21st AIAA Computational Fluid Dynamics Conference*, San Diego, CA, Jul. 2013.
- ¹¹D Arnal and G Casalis. Laminar-turbulent transition prediction in three-dimensional flows. *Progress in Aerospace Sciences*, 36(2):173–191, 2000.
- ¹²Andreas Krumbein. Automatic transition prediction and application to high-lift multi-element configurations. *Journal of aircraft*, 42(5):1150–1164, 2005.
- ¹³Andreas Krumbein, Normann Krimmelbein, and Geza Schrauf. Automatic transition prediction in hybrid flow solver, part 1: Methodology and sensitivities. *Journal of Aircraft*, 46(4):1176, 2009.
- ¹⁴Andreas Krumbein, Normann Krimmelbein, and Geza Schrauf. Automatic transition prediction in hybrid flow solver, part 2: practical application. *Journal of Aircraft*, 46(4):1191, 2009.
- ¹⁵Robin B Langtry and Florian R Menter. Correlation-based transition modeling for unstructured parallelized computational fluid dynamics codes. *AIAA journal*, 47(12):2894–2906, 2009.
- ¹⁶Jae Hoon Choi and Oh Joon Kwon. Enhancement of a correlation-based transition turbulence model for simulating crossflow instability. *AIAA Journal*, 53(10):3063–3072, 2015.
- ¹⁷Loic Jecker, Olivier Vermeersch, Hugues Deniau, Grégoire Casalis, and Emma Croner. A new laminar kinetic energy model for rans simulations of bypass transition. In *47th AIAA Fluid Dynamics Conference*, page 3457, 2017.
- ¹⁸James G Coder. *Development of a CFD-compatible transition model based on linear stability theory*. The Pennsylvania State University, 2014.
- ¹⁹Frédéric Moens, Jean Perraud, Andreas Krumbein, Thomas Toulorge, Pierluigi Iannelli, Peter Eliasson, and Ardeshir Hanifi. Transition prediction and impact on a three-dimensional high-lift-wing configuration. *Journal of Aircraft*, 45(5):1751–1766, 2008.
- ²⁰ROBERTE MAYLE. The role of laminar-turbulent transition in gas turbine engines. In *(ASME, International Gas Turbine and Aeroengine Congress and Exposition, 36 th, Orlando, FL, June 3-6, 1991)* ASME, Transactions, *Journal of Turbomachinery*, volume 113, pages 509–537, 1991.
- ²¹Zhoujie Lyu, Gaetan KW Kenway, and Joaquim RRA Martins. Aerodynamic shape optimization investigations of the common research model wing benchmark. *AIAA Journal*, 53(4):968–985, 2014.
- ²²Gaetan KW Kenway, Ney Secco, Joaquim RRA Martins, Asitav Mishra, and Karthik Duraisamy. An efficient parallel overset method for aerodynamic shape optimization. In *Proceedings of the 58th AIAA/ASCE/AHS/ASC Structures, Structural Dynamics, and Materials Conference, AIAA SciTech Forum, Grapevine, TX*, 2017.
- ²³Gaetan KW Kenway. *A Scalable, Parallel Approach for Multi-Point, High-Fidelity Aerostructural Optimization of Aircraft Configurations*. PhD thesis, University of Toronto (Canada), 2013.
- ²⁴Philippe R Spalart, Steven R Allmaras, et al. A one equation turbulence model for aerodynamic flows. *RECHERCHE AEROSPATIALE-FRENCH EDITION*-, pages 5–5, 1994.
- ²⁵Mujeeb R Malik and Steven A Orszag. Linear stability analysis of three-dimensional compressible boundary layers. *Journal of Scientific Computing*, 2(1):77–97, 1987.
- ²⁶Tuncer Cebeci. *Analysis of turbulent boundary layers*, volume 15. Elsevier, 2012.
- ²⁷G Schrauf. Transition prediction using different linear stability analysis strategies. In *12th Applied Aerodynamics Conference*, page 1848, 1994.

- ²⁸Hans W Stock. en transition prediction in three-dimensional boundary layers on inclined prolate spheroids. *AIAA journal*, 44(1):108–118, 2006.
- ²⁹JD Crouch, LL Ng, YS Kachanov, VI Borodulin, and AV Ivanov. Influence of surface roughness and free-stream turbulence on crossflow-instability transition. *Procedia IUTAM*, 14:295–302, 2015.
- ³⁰N Marković, C Christiansen, AM Mack, WH Huber, and AM Goldman. Superconductor-insulator transition in two dimensions. *Physical Review B*, 60(6):4320, 1999.
- ³¹Andreas Krumbein. Transitional flow modeling and application to high-lift multi-element airfoil configurations. *Journal of aircraft*, 40(4):786–794, 2003.
- ³²J Dagenhart and William S Saric. Crossflow stability and transition experiments in swept-wing flow. 1999.
- ³³J Barche. Pressure distributions on the onera-m6-wing at transonic mach numbers. *AGARD AR-138*, 1979.
- ³⁴Daisuke Yorita, Keisuke Asai, Christian Klein, Ulrich Henne, and Sven Schaber. Transition detection on rotating propeller blades by means of temperature-sensitive paint. In *50th AIAA Aerospace Sciences Meeting including the New Horizons Forum and Aerospace Exposition*. Nashville, TN, 2012.